On the spin-temperature evolution during the epoch of reionization

Rajat M. Thomas[1,2,3][*], Saleem Zaroubi[1,4]

[1] *Kapteyn Astronomical Institute, University of Groningen, P.O. Box 800, 9700 AV Groningen, the Netherlands.*
[2] *Institute for the Mathematics and Physics of the Universe (IPMU), The University of Tokyo, Chiba, 277-8582, Japan.*
[3] *CITA, University of Toronto, 60. St. George Street, M5S 3H8, Toronto, ON, Canada.*
[4] *Physics Department, Technion, Haifa 32000, Israel.*

ABSTRACT

Simulations estimating the brightness temperature (δT_b) of the redshifted 21-cm from the epoch of reionization (EoR) often assume that the spin temperature (T_s) is decoupled from the background CMB temperature and is much larger than it, i.e., $T_s \gg T_{CMB}$. Although a valid assumption towards the latter stages of the reionization process, it does not necessarily hold at the earlier epochs. Violation of this assumption will lead to fluctuations in δT_b that are neither driven by density fluctuations nor by H_{II} regions. Therefore, it is vital to calculate the spin temperature self-consistently by treating the Lyα and collisional coupling of T_s to the kinetic temperature, T_k. In this paper we develop an extension to the BEARS algorithm, originally developed to model reionization history, to include these coupling effects. Here we simulate the effect in ionization and heating for three models in which the reionization is driven by stars, miniqsos or a mixture of both. We also perform a number of statistical tests to quantify the imprint of the self-consistent inclusion of the spin temperature decoupling from the CMB. We find that the evolution of the spin temperature has an impact on the measured signal specially at redshifts higher than 10 and such evolution should be taken into account when one attempts to interpret the observational data.

Key words: Physical data processes: radiative transfer – cosmology: theory – observation – diffuse radiation – radio lines: general.

1 INTRODUCTION

Physical processes that occur during reionization are numerous and complex. Nevertheless, ionization of neutral gas (hydrogen & helium) and heating of the inter-galactic medium (IGM) can be considered the two primary influences of radiating objects during reionization.

Currently, the most promising "direct" probe of reionization is the redshifted 21-cm radiation emanating from neutral hydrogen during the epoch of reionization (EoR), which are to be measured using upcoming telescopes like LOFAR[1,2], MWA[3], PAPER[4] and 21CMA[5]. The intensity of the observed 21-cm radiation depends on the ratio between the number density of electrons in the hyperfine states in the ground state of a neutral hydrogen atom. This ratio is normally expressed in terms of the so-called 21-cm spin temperature, T_s. At the onset of the formation of the first reionizing objects the spin temperature is equal to the CMB temperature since

at these redshifts the ratio between excited and ground hyperfine state electrons is completely determined by the CMB. However, as the number of ionizing sources increases, T_s starts departing from T_{CMB}; slowly at the beginning, then rapidly approaching values larger than T_{CMB}. This evolution is typically ignored in most previous studies of reionization which assumes $T_s \gg T_{CMB}$ at all times (Mellema et al. 2006; Abel & Norman 2000, 2002; Bromm et al. 2002; Yoshida et al. 2003).

Recently, Baek et al. (2009) have relaxed this assumption on T_s at the dawn of reionization and explored its impact on the brightness temperature. They found a considerable considerable deviation from assuming $T_s \gg T_{CMB}$ at the beginning of reionization. Towards the end of reionization though, this assumption holds ground. But, in order to track the evolution of T_s accurately, like in Baek et al. (2009), it is necessary to perform a detailed 3-D Lyα radiative transfer calculation. The Lyα photons undergo a large number ($\sim 10^5$) of scatterings even in a marginally neutral medium before it is sufficiently off line-centre to "free stream". The scattering angle after each encounter is completely random and therefore the radiative transfer is often done in a Monte Carlo sense (Tasitsiomi 2006; Baek et al. 2009; Pierleoni et al. 2009; Laursen et al. 2009) to capture this random nature of Lyα scatterings.

Unfortunately these Monte Carlo radiative transfer schemes are computationally very expensive, especially if we need to sim-

ulate large fields of view necessary to generate mock data sets for next generation radio telescopes. In order to circumvent the need to perform such computer-intensive calculations to obtain T_s, we develop an algorithm along the lines of BEARS (Thomas et al. 2009) as an approximation. In this paper we present an algorithm that follows the decoupling of T_s from T_{CMB} owing to Lyα photons, which couples the spin temperature to the colour/kinetic temperature via the Wouthuysen-Field effect (Wouthuysen 1952). Collisional excitation and heating caused by secondary electrons resulting from hard X-ray radiation are also included. The dominant source of Lyα flux is the background created by the redshifting of photons in the Lyman band into Lyα. These photons are blueward of Lyα and is injected into Lyα at some distance away from the source.

The amount of intrinsic Lyα, ionizing and "heating" photons is a function of the source spectral energy distribution (SED). Thus the evolution of the spin temperature critically depends on the source of reionization. Different reionization sources manifest themselves by influencing the IGM in markedly different ways. For example, deficiency of hard photons in the SEDs of "first stars", limit the extent to which they heat the IGM (Thomas & Zaroubi 2008; Zaroubi et al. 2007; Zaroubi & Silk 2005), while miniquasars (or miniqsos, characterized by central black hole masses less than a million solar), abundant in X-ray photons, cause considerable heating (Madau, Meiksin, & Rees 1997; Ricotti & Ostriker 2004; Nusser 2005; Furlanetto, Zaldarriaga, & Hernquist 2004; Wyithe & Loeb 2004; Furlanetto & Loeb 2002; Thomas & Zaroubi 2008; Zaroubi et al. 2007). Ionization profiles similarly have their characteristic source-dependent behavior.

Although the question on which sources did the bulk of the reionization is up for debate, it is conceivable from observations of the local Universe up to redshifts around 6.5, that sources of reionization could have been a mixture of both stellar and quasar kinds (their respective roles again are uncertain). Implementing radiative transfer that include both ionizing and hard X-ray photons has been difficult and as a result most 3-D radiative transfer schemes restrict themselves to ionization due to stars (Gnedin & Abel 2001; Ciardi et al. 2001; Ritzerveld, Icke, & Rijkhorst 2003; Susa 2006; Razoumov & Cardall 2005; Nakamoto, Umemura,& Susa 2001; Whalen & Norman 2006; Rijkhorst et al. 2006; Mellema et al. 2006; Zahn et al. 2007; Mesinger & Furlanetto 2007; Pawlik & Schaye 2008). In Ricotti & Ostriker (2004), a "semi" hybrid model of stars and miniqsos, like the one hinted above, has been used albeit in sequential order instead of a simultaneous implementation. That is, pre-ionization due to miniqsos was invoked between $7 \leqslant z \leqslant 20$, after which, stars reionize the Universe at redshift 7. We in this paper would like to address the issue of simulating the propagation of both the UV and hard X-ray photons, exactly in 1-D and as approximation in 3-D.

The focus of this paper is therefore to introduce the algorithm that is used to implement IGM heating in BEARS along with the procedure to estimate the spin temperature of the IGM. As an application of this technique we explore the effects of heating due to miniqsos, stars and, for the first time, a mixed "hybrid population". Subsequently, we provide quantitative and qualitative analysis of the differences in the 21-cm EoR signal with and without the usual assumption of T_s being always decoupled from T_{CMB}.

The paper is organized as follows; §2 describes briefly the N-body and 1-D radiative transfer codes used. In §3 we describe the adaptation of BEARS to include T_k, followed by the calculation of the T_s and δT_b within the simulation box. BEARS is then applied to three different scenarios of reionization in §4, *viz.*, (1) the primary

source being stars, (2) miniqsos and (3) a hybrid population of stars and miniqsos. Subsequently, observational cubes of δT_b are generated for each of these scenarios and its properties discussed. In §5 we provide statistics on the simulated boxes and interpret the finding mainly from the point of view of the differences in δT_b with and without the usual assumption that T_s is decoupled from T_{CMB}. We also compare our work to that of Santos et al. (2008) in the same section. Conclusions and discussions of the results are presented in §6, along with a mention of a few topics that can be addressed using the data set simulated in this paper.

2   SIMULATIONS

In this section we briefly mention the dark-matter-only N-body simulations employed, the 1-D radiative transfer code developed by Thomas & Zaroubi (2008) and provide an overview of the BEARS algorithm designed in Thomas et al. (2009).

2.1   N-body: dark matter only

The dark matter only N-body simulations are the same as in Thomas et al. (2009) and was performed by Joop Schaye and Andreas Pawlik at the Leiden observatory. The N-body/TreePM/SPH code GADGET (Springel 2005) was used to perform a dark matter (DM) cosmological simulation containing 512^3 particles in a box of size 100 h^{-1} comoving Mpc with each DM particle having a mass of 4.9×10^8 h^{-1} M$_\odot$.

Initial conditions for the particle's position and velocity were obtained from glass-like initial conditions using CMBFAST (version 4.1; Seljak & Zaldarriaga (1996)) and the Zeldovich approximation was used to linearly evolve the particles down to redshift z = 127. A flat ΛCDM universe is assumed with the set of cosmological parameters $\Omega_m = 0.238$, $\Omega_b = 0.0418$, $\Omega_\Lambda = 0.762$, $\sigma_8 = 0.74$, $n_s = 0.951$ and $h = 0.73$ (Spergel et al. 2007). Snapshots were written out at 35 equally spaced redshifts between $z = 12$ and $z = 6$. Halos were identified using the Friends-of-Friends algorithm (Davis et al. 1985), with linking length $b = 0.2$. The smallest mass haloes we can resolve are a few times 10^{10} h^{-1} M$_\odot$. The density field was smoothed on the mesh with a Gaussian kernel with standard deviation $\sigma_G = 2 \times 100/512$ comoving Mpc/h (2 grid cells).

2.2   1-D radiative transfer (RT) code.

The implementation of the 1-D radiative transfer code is modular and hence straightforward to include different spectra corresponding to different ionizing sources. Our 1-D code can handle X-ray photons, the secondary ionization and heating it causes, and as a result perform well both for high (quasars/miniqsos) and low energy (stars) photons. Further details of the code can be found in Thomas & Zaroubi (2008).

The parameter space simulated by the 1-D radiative transfer scheme (Thomas & Zaroubi 2008) include; 1) different SEDs (stars or miniqsos with different power-law indices), 2) duration of evolution (depending on the life-time of the source), 3) redshifts at which these sources turn on and 4) clumping factor or over-density around a given source. Information on the ionization and temperature profiles from these simulations were cataloged to be used later as in Thomas et al. (2009). Density profiles around sources are assumed to be homogeneous although the code could be initialized using any given profile.

2.3 BEARS algorithm: overview

BEARS is a fast algorithm that simulates the underlying cosmological 21-cm signal from the EoR. It is implemented by using the Nbody/SPH simulation in conjunction with a 1-D radiative transfer code; both discussed in the previous sections. The basic steps of the algorithm are as follows: first, a catalogue of 1-D ionization profiles of all atomic hydrogen and helium species and the temperature profile that surround the source is calculated for different types of ionizing sources with varying masses, luminosities at different redshifts. Subsequently, photon rates emanating from dark matter haloes, identified in the N-body simulation, are calculated semi - analytically. Finally, given the spectrum, luminosity and the density around the source, a spherical ionization bubble is embedded around the source, whose radial profile is selected from the catalogue as generated above. In case of overlap between ionization bubbles, the excess ionized atoms in the overlap area is redistributed at the edge of the bubbles. For more details see Thomas et al. (2009). The outputs are data cubes (2-D slices along the frequency/redshift direction) of density (δ), radial velocity (v_r) and hydrogen and helium fractions ($x_{HI;HII;HeI;HeII\&HeIII}$). Each data cube consists of a large number of slices each representing a certain redshift between 6 and 11.5. Because these slices are produced to simulate a mock dataset for radio-interferometric experiments, they are uniformly spaced in frequency (therefore, not uniform in redshift). Thus, the frequency resolution of the instrument dictates the scales over which structures in the Universe are averaged/smoothed along the redshift direction. The relation between frequency and redshift space z is given by:$z = \frac{\nu_{21}}{\nu} - 1$, where $\nu_{21} = 1420$ MHz is the rest frequency that corresponds to the 21-cm line.

3 INCLUDING IGM HEATING IN BEARS

In Thomas et al. (2009) the BEARS algorithm was introduced; a special-purpose 3-D radiative transfer scheme used to simulate cosmological EoR signals. In that paper we detailed the philosophy behind the code and its implementation to incorporate ionization due to a variety of sources. In this section, we extend the features of BEARS to include heating (on which the brightness temperature is sensitively dependent) due to hard photons within the same framework.

The algorithm to implement heating begins in a manner similar to that for ionization. The T_k-profile from the 1-D radiative transfer code is used to embed a spherically symmetric "T_k bubble" at the locations of the centre-of-mass of dark matter haloes. The luminosity of the source is a function of the halo mass. The problem embedding a temperature profile in the simulation box is that, the radius of the bubble is large (> 5 Mpc) and results in extensive overlap, even at high redshifts; a problem encountered for ionization bubbles only towards the end of reionization. In a quasar dominated part of the Universe this is particularly severe because of its large sphere-of-influence in heating the IGM.

3.1 Treating overlaps: Energy conservation

Overlap in the spheres of ionized regions was treated by redistributing the excess ionizing photons in the overlapped region uniformly around the overlapping spheres (Thomas et al. 2009). Treating overlapped zones directly in terms of temperatures makes it difficult to come up with any "conserved quantity". To elaborate, consider a pre-ionized zone in the simulation box close to the radiating source. Although at close proximity to the source, this region is not heated efficiently because of the absence of neutral hydrogen to capture the photons. On the other hand, the same source can dump more energy into an initially neutral zone that maybe far away from it. Thus, embedding the T_k-profile directly from the catalog (which assumes uniform IGM density) is not appropriate.

Here we adopt a different approach where we estimate the total energy deposited in every region of the simulation box and invoke the conservation of energy deposited by the sources in the overlapped regions. We integrate the contribution to the energy budget, at a given location, from all sources whose sphere-of-influence extents to that location. This total energy is then redistributed equally to all the contributing sources, i.e., the energy output of each source is modified to account for the overlapping.

To illustrate, consider $\mathcal{N}$ sources that overlap at a particular location $\vec{r}$ and the total energy estimated at that location to be $E_{tot} = \sum_{i=1}^{N} E_i$, where E_i is the energy deposited by the ith source at location $\vec{r}$. The fraction of "excess" energy attributed to each of the $\mathcal{N}$ sources is $\delta E = E_{tot}/\mathcal{N}$. This energy δE is then added to the total energy from the source to estimate a new normalization constant for the SED of the source. For example in case of a power-law-type source, the SED includes a normalization term that is determined by the total energy of the source, E_{total}. However, in the overlap case the total energy of the source is replaced by $E_{total} + \delta E$. Now a "new" bubble of kinetic temperature is embedded whose profile depends on a source whose output energy has gotten a δE boost. In this manner $T_k(\vec{r})$ is estimated at every location in the simulation box. From this point on we need to estimate the coefficients that couple T_k to T_s that will eventually lead to the estimation of δT_b. It is worthwhile also to note that the results are robust to variation in the exact algorithm used to treat the overlapped region. For example, if we choose to sum the energies deposited directly in a given region or choose $\max(E_1, E_2, ..., E_n)$, where $E_1...E_n$ are energies deposited by sources 1...n respectively, the final results are very similar.

This is obviously an approximation which assumes that the efficiency of the photons in heating the IGM does not depend on their frequency. For the case of power-law sources where most of the energy comes from hard photons this is probably a reasonable approximation. However, in the case of blackbody sources this is not a very good assumption because evidently the heating is done by a very small fraction of photons. But in these cases the overlap problem is not as severe as for the power-law sources since the extent of the heating is much more limited. In summary, despite the approximate nature of this approach, it provides an efficient and reasonable resolution for the issue of the overlapping of temperature bubbles. We note that self consistent treatment of this problem requires taking into account the modification of each of sources' SED in a different manner depending on the amplitude of its SED. Obviously this is computationally very expensive.

3.2 Calculating δT_b in the volume

Spin temperature can be thought of as a short hand notation to represent the level population of the hyperfine states of the ground level of a hydrogen atom. Depending on the physical processes and background radiation that dominate a medium, T_s is either coupled to the background CMB temperature or to the kinetic temperature of the hydrogen gas in the medium. Formally Field (1958) derived T_s as a weighted sum of T_k and T_{CMB}, as;

$$T_s^{-1} = \frac{T_{CMB}^{-1}(z) + y_\alpha T_k^{-1} + y_{coll} T_k^{-1}}{1 + y_\alpha + y_{coll}}, \tag{1}$$

where y_α and y_{coll} are parameters that reflect the coupling of T_s to T_k via Lyα excitation and collisions respectively. The efficiency of Lyα-coupling dominates over that of collisions, especially further away from the source (Thomas & Zaroubi 2008; Chuzhoy, Alvarez, & Shapiro 2006). In our treatment of calculating T_s, we estimate both y_α and y_{coll}.

The coefficient y_{coll} is a function of T_k and the ionized fraction of the medium, x_{HII}. These informations on ionization and heating are available from the prescription outlined in the previous section. While simulating the 1-D profiles we simultaneously calculate y_α as;

$$y_\alpha = \frac{16\pi^2 T_\star e^2 f_{12} J_o(|r|)}{27 A_{10} T_e m_e c}. \tag{2}$$

Here, $J_o(|r|)$ is the Lyα flux density at distance r from the source. For miniqsos with high energy photons, Lyα coupling is mainly caused by collisional excitation due to secondary electrons (Chuzhoy, Alvarez, & Shapiro 2006). This process is accounted for by the following integral,

$$J_o(|r|) = \frac{c}{4\pi H(z)\nu_\alpha} n_{HI}(r) \int_{50eV}^{2KeV} \phi_\alpha(E)\sigma(E)N(E;r,t)dE, \tag{3}$$

where $N(E;r;t)$ is the number of photons with energy 'E' at radius 'r', and time 't' per unit area (Zaroubi & Silk 2005). This number is obtained directly from the 1-D radiative transfer by taking into account the the absorption due to the optical depth along the line-of-sight to the source at a distance 'r'. The 1-D profiles generated are catalouged also as a function of time. Therefore the profiles that are embedded within the simulation are chosen to obey causality [6]. The ionization cross-section of neutral hydrogen in the ground state is given by $\sigma(E)$, $f_{12} = 0.416$ is the oscillator strength of the Lyα transition, e & m_e are the electron's charge and mass, respectively, ϕ_α is the fraction of the absorbed photon energy that goes into excitation (Shull & van Steenberg 1985; Dijkstra, Haiman, & Loeb 2004). Note here that the fitting formula is a function of both ionization fraction and energy as given in the appendix of Dijkstra, Haiman, & Loeb (2004).

For the case of stars, the dominant source of Lyα flux results from the redshifting of the source spectrum blueward of Lyα into the resonant line at different distances from the source. Frequency 'ν' at the redshift of emission (or the source) 'z' is redshifted into $\nu_{Ly\alpha}$ at redshift $z(|r|)$ such that;

$$\nu = \nu_{Ly\alpha} \frac{1+z}{1+z(|r|)}. \tag{4}$$

Thus, at every radius r away from the source the Lyα flux $J_o(|r|) \propto N(E';r;t)/r^2$. Where $E' = 10.2 \frac{1+z}{1+z(|r|)}$ [eV].

Now, instead of embedding a sphere of the T_s, as in the case of T_k, we embed instead the a bubble of Lyα flux, $J_o(|r|)$, as estimated from Eq. 3. Since $J_o(|r|)$ is basically the number of Lyα photons at a given location, the overlap of two "J$_o$ bubbles" implies that the photons and hence the J$_o$ has to be added, i.e., at a given spatial (pixel) location, $\vec{x}$, $\vec{y}$, $\vec{z}$ and time t, the total Lyα flux is given by;

---

[6] Of course the catalouge has been generated with a a particular time resolution and can be made finer for more accurate results

$$J_o^{tot}(\vec{x}, \vec{y}, \vec{z}, t) = \sum_{i=0}^{N} J_o^i(\vec{x}, \vec{y}, \vec{z}, t), \tag{5}$$

where $J_o^i(\vec{x}, \vec{y}, \vec{z}, t)$ is the Lyα flux contributed by i^{th} source at the pixel location in the box, $\vec{x}$, $\vec{y}$, $\vec{z}$ and time t. Equipped with the quantities $T_k(\vec{r})$, and $J_o(\vec{r})$, we can calculate y_α as in Eq. 2, and subsequently the spin temperature through Eq. 1. Now all terms required for the calculation of δT_b, as in Eq. 6, are obtained.

$$\delta T_b(\vec{r}) = (20 \text{ mK}) (1 + \delta(\vec{r})) \left(\frac{x_{HI}(\vec{r})}{h}\right) \left(1 - \frac{T_{CMB}}{T_s(\vec{r})}\right)$$
$$\times \left[\frac{H(z)/1+z}{dv_{||}/dr_{||}}\right] \left(\frac{\Omega_b h^2}{0.0223}\right) \left[\left(\frac{1+z}{10}\right)\left(\frac{0.24}{\Omega_m}\right)\right]^{1/2} \tag{6}$$

4 EXAMPLE APPLICATIONS OF BEARS

In this section we apply BEARS with its extended feature of including heating of the IGM, to three different scenarios of reionization. The models described in this section are not "template" reionization scenarios by any measure nor is any particular model favoured w.r.t the other. In fact, these models may be far from reality and only serve as examples of the potential of BEARS to provide a reasonable estimate of the 21-cm brightness temperature for widely different scenarios of reionization.

4.1 Heating due to stars

The first scenario explored using BEARS is the case in which the sources of reionization are *only* stars. In this section we describe the model used to describe the stellar component and the prescription adopted to embed these stars into haloes of dark matter identified in an N-body simulation.

4.1.1 *Modeling stellar radiation in* BEARS

Most stars, to first order, behave as blackbodies at a given temperature, although the detailed features in the SED depends on more complex physical processes, age, metallicity and mass of the star. This blackbody nature imprints characteristic signatures on the IGM heating and ionization patterns (Thomas & Zaroubi 2008). Schaerer (2002) showed that the temperature of the star only weakly depends on its mass. The blackbody temperature of the stars in our simulation was thus fixed at 5×10^4 K to perform the radiative transfer. We sample the parametre space of redshifts (12 to 6), density profiles around the source [7] and masses (10 to 1000 $M_\odot$). The total luminosity is normalized depending on the mass of the star according to Table. 3 in Schaerer (2002).

For blackbody with a temperature around 10^5 K, similar to our adopted value, the spectrum peaks between ≈ 20 eV to ≈ 24 eV (Wien's displacement law). Thus, from the form of the blackbody spectrum we can apriori expect, in the case of stars, that the ionization induced by these objects will be high, but the heating they cause will not be substantial given the exponential cutoff of the radiation towards higher frequencies.

---

[7] We can incorporate any given density profile like the homogeneous, isothermal or NFW profiles. For this paper however we ran all the simulations using a homogeneous background. Overdensities around sources can be corrected for by using the prescribtion in Thomas et al. (2009).

Now, following the prescription in Thomas et al. (2009) we associate stellar spectra with dark matter halos using the following procedure. The global star formation rate density $\dot{\rho_\star}(z)$ as a function of redshift was calculated using the empirical fit;

$$\dot{\rho_\star}(z) = \dot{\rho_m} \frac{\beta \exp[\alpha(z - z_m)]}{\beta - \alpha + \alpha \exp[\beta(z - z_m)]} \ [\mathrm{M_\odot \ yr^{-1} \ Mpc^{-3}}], (7)$$

where $\alpha = 3/5$, $\beta = 14/15$, $z_m = 5.4$ marks a break redshift, and $\dot{\rho}_m = 0.15[\mathrm{M_\odot \ yr^{-1} Mpc^{-3}}]$ fixes the overall normalisation (Springel & Hernquist 2003). Now, if δt is the time-interval between two outputs in years, the total mass density of stars formed is

$$\rho_\star(z) \approx \dot{\rho}_\star(z)\delta t \ [\mathrm{M_\odot \ Mpc^{-3}}]. (8)$$

Notice that this approximation is valid only if the typical lifetime of the star is much smaller than δt, which indeed is the case in our model because the stellar mass we input (100 $\mathrm{M_\odot}$) has a lifetime of about a few Myrs (Schaerer 2002), compared to a typical time difference of few tens of Myrs between simulation snapshots.

Therefore, the total mass in stars within the simulation box is $M_\star(box) \approx L_{box}^3 \rho_\star \ [\mathrm{M_\odot}]$. This mass in stars is then distributed among the halos weighted by their mass;

$$m_\star(halo) = \frac{m_{\mathrm{halo}}}{M_{\mathrm{halo}}(tot)} M_\star(box), (9)$$

where $m_\star(halo)$ is the mass in stars in the dark matter "halo", m_{halo} the mass of the halo and $M_{\mathrm{halo}}(tot)$ the total mass in halos within the simulation box.

We then assume that all of the mass in stars is distributed in stars of 100 $\mathrm{M_\odot}$, which implies that the number of stars in the halo is $N_{100} = 10^{-2} \times m_\star(halo)$. The luminosity of a 100 $\mathrm{M_\odot}$ star is obtained from Fig. 1 of Schaerer (2002), assuming zero metallicity. The luminosity of 100 $\mathrm{M_\odot}$ star thus derived is in the range of $10^6 - 10^7 \ L_\odot$ and this value is multiplied by N_{100} to get the total luminosity emanating from the "halo" and the radiative transfer is done by normalizing the blackbody spectrum to this value. The escape fractions of ionizing photons from early galaxies is assumed to be 10%.

4.1.2 Results: Stellar sources

Results of the evolution of the T_k, T_s and δT_b of the IGM, when the sources of reionization comprise only of stars is shown in Figs 1, 2 and 3, respectively.

Figure 1 shows the kinetic temperature for stellar sources at redshifts 10, 8, 7 and 6 at which their ionized fractions are 0.12, 0.5, 0.83, and 0.98 respectively. The blackbody type stellar spectra do not have sufficient high energy photons to heat the IGM substantially far away from the source. Thus we see compact regions (bubbles) of high temperature in the immediate vicinity of the source. In the inner parts, where the ionized fraction is high ($x_{\mathrm{HII}} > 0.95$), the temperatures are of the order of $\approx 10^5$ K and drops sharply in the transition zone to neutral IGM. The ionized region is restricted to about 100 kpc in physical coordinates around a halo (Thomas & Zaroubi 2008).

Figure. 2 shows T_s at four different redshifts. Collisional coupling (y_{coll}) is important close to the radiating source ($< 200 \ kpc$). The primary source of coupling between T_s and T_k is the redshifting of photons blueward of the Lyα line into the Lyα frequency. It has to be emphasized here that the Lyα photons are produced *only* due to the source and secondary processes. Thus we see that stellar sources are efficient in building up a significant background
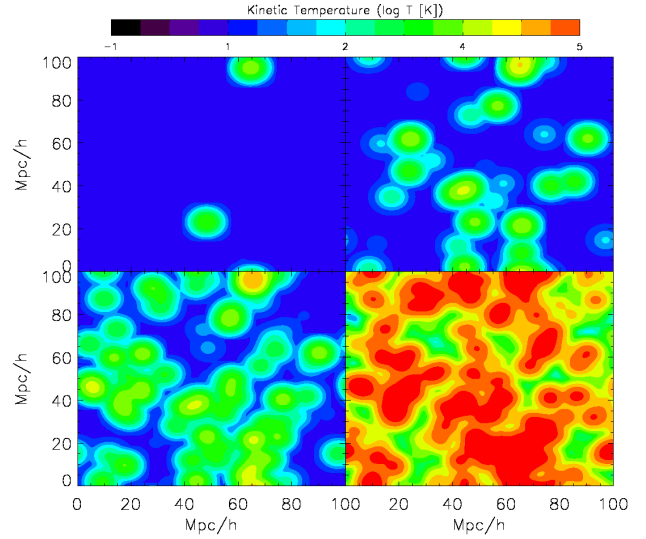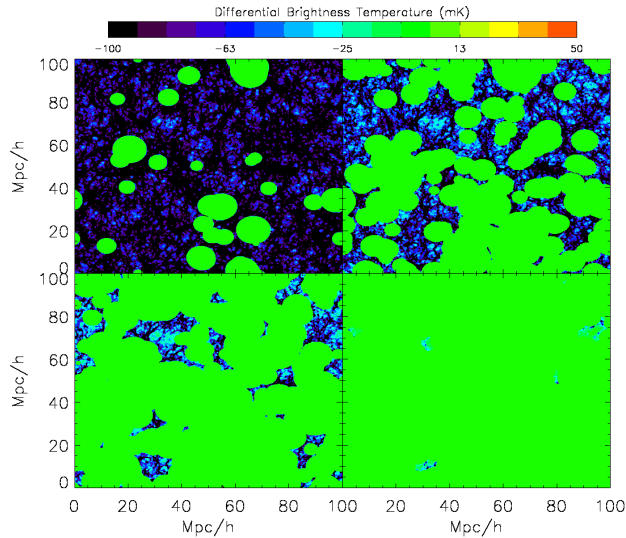

Figure 1. *Kinetic Temperature for stellar sources*: Slices of T_k corresponding to redshifts 10, 8, 7 and 6 are plotted (*panels left to right and top to bottom, respectively*). Temperature are indicated in log T [K] on the color bar above. The extent of heating, both in amplitude (maximum around $\approx 10^5$ K towards the center) and spatial extent (< 100 kpc), is extremely small. Basically, only the central part (ionized region) is at a high temperature and falls sharply during the transition into the neutral IGM.
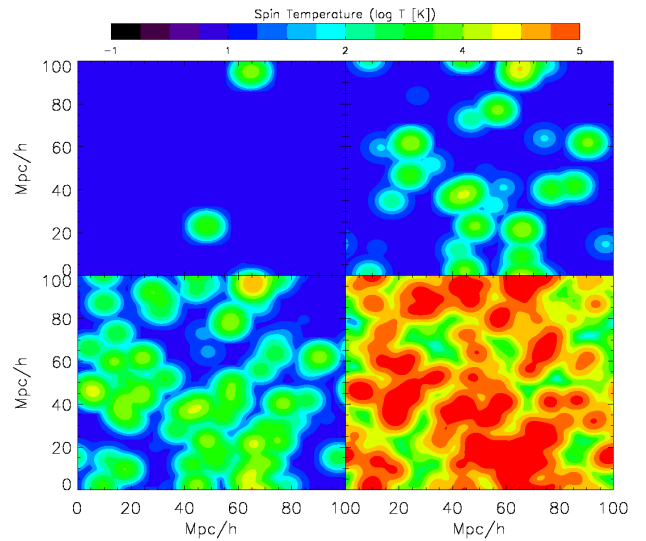
Figure 2. *Spin Temperature for stellar sources*: Slices correspond to that in Fig. 1. Collisional coupling is efficient to couple the T_k to T_s at the centre but the figures also indicate that there is sufficient J_o to couple T_k to T_s well beyond the ionized region, where $T_k < T_{\mathrm{CMB}}$. The color bar indicates temperature on a log T [K] scale.

of J_o far away from the source which is sufficient to couple T_s to T_k during reionization (Ciardi & Madau 2003). As an example, in Fig. 12 we show the reionization history (δT_b) assuming a high background J_o, in other words, assuming perfect T_s—T_k coupling.

In Fig. 3 δT_b corresponding to the same redshifts as in the previous figures is shown. In this particular model δT_b values are not very high ($|\delta T_b| < 10$mK). At early epochs, (top-left) at $z \approx 10$, there are only a few sources and the heating of the IGM or the secondary J_o is not high enough to cause substantial differential brightness temperatures. At later times, the ionized bubbles over-

Figure 3. *Differential Brightness Temperature for stellar sources*: Slices corresponds to that in Fig. 1. The temperature is now contoured on a linear scale with values indicated on the colorbar. In these slices, δT_b, starting from zero within ionized regions attains large negative value outside because stars are not efficient at heating the IGM beyond their ionized bubble and hence cannot render the IGM visible in emission. Early on, (top-left) at a redshift of 10, there are only a few sources and the heating induced collisional coupling or the J_o is not high enough to render the Universe visible, but the photons blueward of Lyα can reach far outside the ionized region where they are injected into Lyα frequency causing substantial coupling to the kinetic temperature which is much below the CMB. And, at later times, the ionized bubbles overlap significantly driving the brightness temperature to zero.

lap significantly driving the brightness temperature to zero. Thus there is only a small portion of the Universe (in volume) that has sufficient Lyα coupling and neutral hydrogen density to cause large differential brightness temperatures. This behaviour is specific to the model assumed and will be significantly different if the parameters such as the star-formation rate, SED and escape fractions are altered.

4.2 Heating due to miniqsos

In this section we will consider heating due to high energy X-ray photons emanating from power-law type sources (eg., miniqsos). Because of their large mean free path ($\propto E^3$) it has been difficult to incorporate the effect of heating by power-law sources self-consistently in a 3-D radiative transfer simulation.

4.2.1 Modeling miniqsos in BEARS

Observations reveal the energy spectrum of quasars-type sources typically follow a power-law of the form $E^{-\alpha}$ (Vanden Berk et al. 2001; Vignali, Brandt, & Schneider 2003; Laor et al. 1997; Elvis et al. 1994). Here we assume $\alpha = 1$ and thus the SED of the miniqsos is given by:

$$I(E) = Ag \times E^{-\alpha} \quad 10.4\,\mathrm{eV} < E < 10^4\,\mathrm{eV}, \tag{10}$$

with the normalization constant,

$$Ag = \frac{E_{total}}{\int\limits_{E_{range}} I(E)\mathrm{dE}}, \tag{11}$$

where E_{total} is the total energy output of the miniqso within the energy range, E_{range}. Any complex, multi-slope spectral templates as in Sazonov, Ostriker, & Sunyaev (2004) can be adopted. The number of plausible SEDs that can be considered are numerous and serves as a reminder of the extent of "unexplored parameter space" even while considering the case of miniqsos alone, and argues for an extremely quick RT code like BEARS.

The miniqsos are assumed to accrete at a constant fraction ϵ (normally 10%) of the Eddington rate. Therefore, the luminosity is given by:

$$L = \epsilon\,L_{\mathrm{edd}}(M) \tag{12}$$

$$= 1.38 \times 10^{37} \left(\frac{\epsilon}{0.1}\right)\left(\frac{M}{M_\odot}\right)\mathrm{erg\ s^{-1}}. \tag{13}$$

The luminosity derived from the equation above is used to normalize the relation in Eq. 10 according to Eq. 11. The energy range considered is between 10.4 eV and 10 keV. Simulations were carried out for a range of masses between 10^5 and 10^9 $M_\odot$. To justify comparing the case of stars and miniqsos we argue that, although the number of photons at different energies is a function of the total luminosity and spectral index in the case of miniqsos, if we assume that all photons from the miniqso are at the hydrogen ionization threshold, then the number of ionizing photons obtained, for the mass range fixed above, is about 10^{50} to 10^{55}; the same order of magnitude as the number of ionizing photons in the case of stars and it also matches the numbers being employed for simulations by various other authors like Mellema et al. (2006) and Kuhlen & Madau (2005).

The miniqsos are embedded into an N-body output following the prescription in Thomas et al. (2009). Dark-matter haloes are identified using the friends-of-friends (FoF) algorithm and masses of black holes assigned according to,

$$M_{\mathrm{BH}} = 10^{-4} \times \frac{\Omega_b}{\Omega_m} M_{halo}, \tag{14}$$

where the factor 10^{-4} reflects the Magorrian relation (Magorrian et al. 1998) between the halo mass (M_{halo}) and black hole mass (M_{BH}) multiplied with the radiative efficiency assumed to be 10%, and the fraction $\frac{\Omega_b}{\Omega_m}$ gives the baryon ratio (Ferrarese 2002).

4.2.2 Results: miniqsos

Contour plots of T_k, T_s and and δT_b for the case of *only* miniqsos being the sources of reionization, at four different redshifts, are plotted in Figs. 4, 5 and 6, respectively. The high energies of the X-ray photons substantially affects the photo-ionization and thermal energy balance of the IGM.

The marked difference between power-law type and stellar sources, in the extent to which they heat the IGM, is evident in Fig. 4. The temperatures are shown at redshifts 10, 8, 7 and 6 with ionized fractions 0.01, 0.54, 0.96, 0.999 respectively. In the inner parts of the "T_k bubble" the amplitude of T_k is about $\approx 10^{6.5}$ K. The secondary electrons created by high energy X-ray radiation thermalizes to these high temperature values. Also contributing to extremely high temperatures in the very inner parts of the bubble is Compton heating (Thomas et al. 2009). The mean free path of X-rays are extremely large resulting in a spatial extent of heating that reaches many Mpcs. Thus, we see that already at redshift 10 (top-left) the average temperature of the IGM is of the order of 10^3 K and overlap of the temperature bubbles occur much before that of the ionization bubble. This example might be unrealistic, because
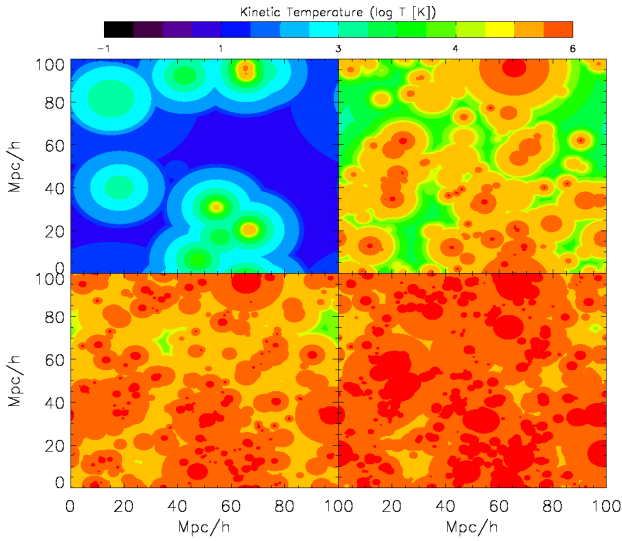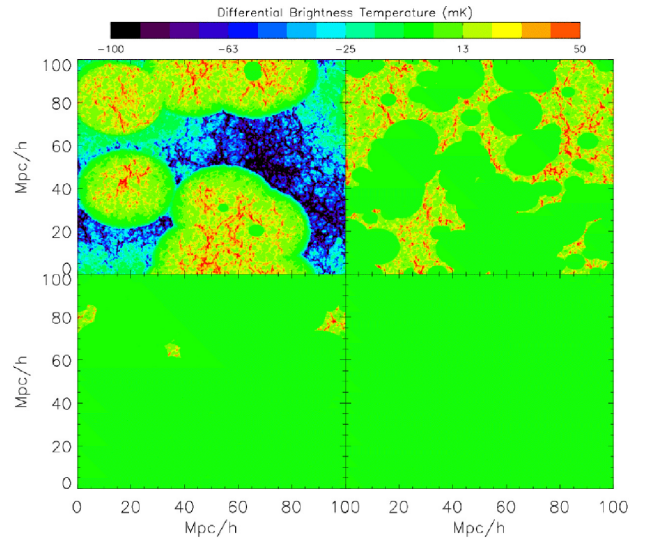
Figure 4. *Kinetic Temperature for miniqso sources*: Slices correspond to that in Fig. 1 with temperatures indicated on a log T [K] scale. Here we see the striking difference between miniqsos and stars in the extent of heating. The amplitude is about $\approx 10^{6.5}$ K towards the center and spatial extent of the heating is about a few Mpcs. Already at redshift 10 (top-left) the average temperature is of the order 10^3 K.
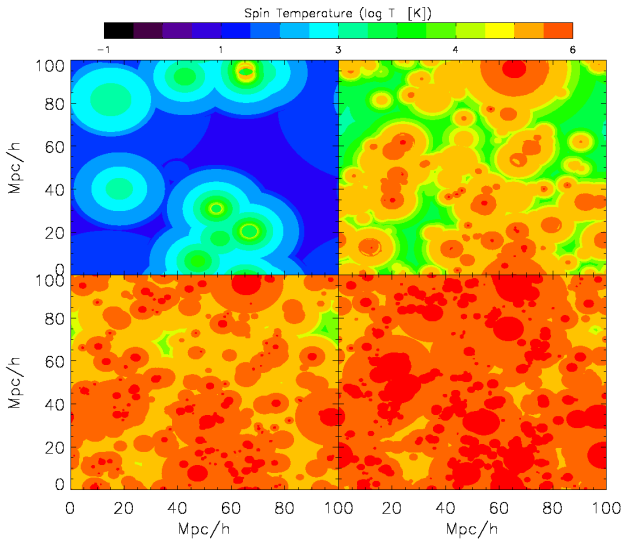
Figure 5. *Spin Temperature for miniqso sources*: Slices correspond to that in Fig. 1 with the temperatures indicated on a log T [K] scale. Spin temperatures show an interesting ring-like behaviour (easily visible in the top-left panel). The reason for this is discussed in the text.

the soft X-ray background constraint (Dijkstra, Haiman, & Loeb 2004) is not strictly observed, but again this serves just as an illustrative example.

Figure. 5 shows the evolution of T_s as a function of redshift. Owing to a high secondary J_o produced due to X-ray photons, T_s is coupled to T_k for the large part. The snapshots of T_s show a peculiar ring-like behaviour (Refer. Fig. 5). This is because towards the central part of the bubble around the source, the IGM is highly ionized and $J_o \propto x_{HI}$, obtains an extremely low value. On the other hand J_o progressively gets lower away from the source, regions (>5Mpc). Therefore only a relatively narrow zone (few hundred

Figure 6. *Differential Brightness Temperature for miniqso sources*: Slices correspond to that in Fig. 1. Note here that the brightness temperature (mK) in plotted on a linear scale with values as indicated on the color bar. We see again from the top-left panel that although the number of sources in the field are few, they were efficient in both increasing T_k dramatically and providing sufficient J_o to "light-up" the Universe in 21-cm around them. The spheres in the top-left panel have δT_b of zero because they are highly ionized.

kpcs) in between the ionizing front and regions further out has J_o high enough to decouple T_s from T_{CMB}.

Figure. 6 shows δT_b for redshifts 10, 9, 8 and 7 in panels top-left to bottom-right, respectively. The δT_b plotted in this figure are high enough to be detectable by upcoming telescope's like LOFAR and MWA, whose sensitivities should reach $\delta T_b > 5$mK (Labropoulos et al. 2009). We see in the top-left panel of this figure that even though the number of sources in the field is small, they are efficient in both increasing T_k dramatically and providing sufficient J_o to "light-up" the Universe in the 21-cm differential brightness temperature. The δT_b inside the spheres are zero because they are highly ionized ($x_{HII} > 0.99$).

4.3 Modeling co-evolution of stars & miniqsos

In the observable Universe we know that stars and quasars do co-exist. Although, there are indications of the quasar number-density peaking around redshift two (Nusser & Silk 1993) and declining thereof, there are also measurements by Fan et al. (2006) of high-mass ($> 10^8 M_\odot$) quasars at $z > 6$. This allows us to envisage a scenario of reionization in which stars and quasars (or miniqsos) contributed to the ionization and heating of the IGM in a combined fashion. As a final example-application of BEARS, we present our model of a "hybrid" star-miniqso SED and examine its results on the ionization and heating of the IGM.

4.3.1 The "Hybrid" SED

The uncertainty regarding the properties and distributions of objects during the dark ages allows us to come up with strikingly different ways of incorporating the co-existence of stars and miniqsos. For example, consider that there are $\mathcal{N}$ different haloes within our simulation box. One approach would be to suppose that each of these haloes host both a miniqso and stars, whose
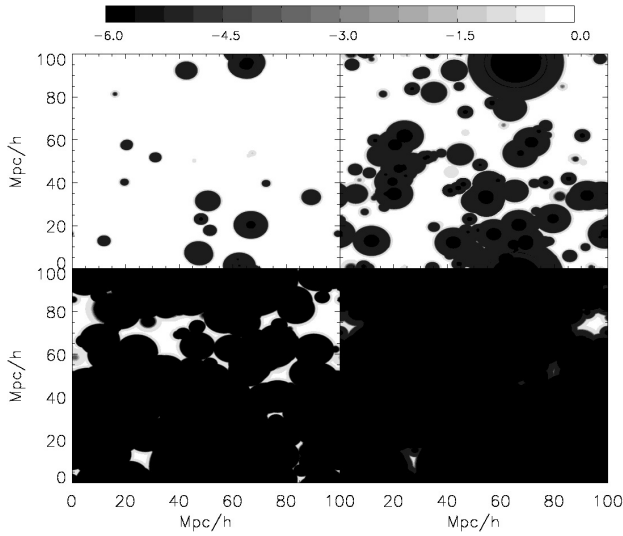
Figure 7. *Ionization due to the hybrid model*: Slices correspond to that in Fig. 1. Shown in these slices are the contour levels of neutral hydrogen in a logarithmic scale. We see here that for the hybrid model we have assumed the ionization proceeds quickly and the Universe is substantially ionized by redshift 6 (Refer Fig. 11) for the reionization history. The extent of ionizations interpolates between the cases of black holes and stars.

Figure 8. *Kinetic temperature for hybrid model*: Slices correspond to that in Fig. 1, with temperatures indicated on a log T [K] scale. The heating pattern is peculiar in that the temperature shows a much "cuspier" behaviour towards the center. The reason is that the stellar component of the source ionized the very central part and the X-ray radiation can thus heat the central part where to even higher temperature. On the other hand the large extent of the heating is attributed to the power-law component of the SED.

Figure 9. *Spin temperature for the hybrid model*: Slices correspond to that in Fig. 1. Spin temperatures for the case of the hybrid model again shows the ring like behaviour as in the case of power-law sources. Temperatures are indicated on a log T [K] scale.

masses/luminosity is derived according to the previous two examples. The other approach would be to place one or two massive miniqsos (almost quasars), still conforming to the black hole mass density predictions of Volonteri, Lodato, & Natarajan (2008), and the rest of the haloes in the simulation box with populations of stars. For this example, given the minimum mass halo our simulation can resolve, we have chosen to adopt the former approach, i.e., a miniqso and stars in every halo.

In our approach, given the halo mass we embed them with stellar sources as described in §4.1.1. Then the black hole mass is set as 10^{-4} times the stellar mass. Radiative transfer is performed using this hybrid SED, i.e., a superposition of power-law type miniqso SED and black body spectrum normalized according to the criterion in the previous sections. The results of ionization and heating are presented below.
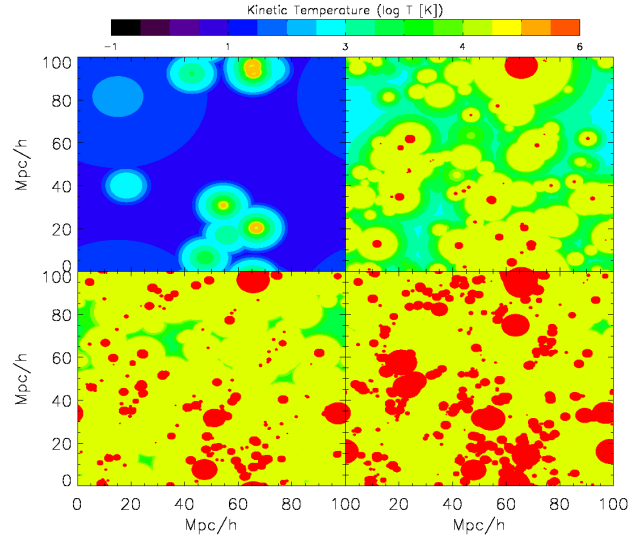
4.3.2   Results: Hybrid model

The hybrid model proposed does have large amounts of high-energy X-ray photons from miniqsos that influence the temperature and ionization of the IGM prior to full reionization. The X-rays photons have larger mean free paths than their UV counterparts, and their secondary electrons have significant influence on the thermal and ionization balance. The UV photons on the other hand are efficient at keeping the IGM in the vicinity of the halo highly ionized. For the redshifts 10, 8, 7 and 6 we plot the ionization due to the hybrid model in Fig. 7 and the ionized fraction at these redshifts are 0.01, 0.38, 0.86 and 0.995 respectively.
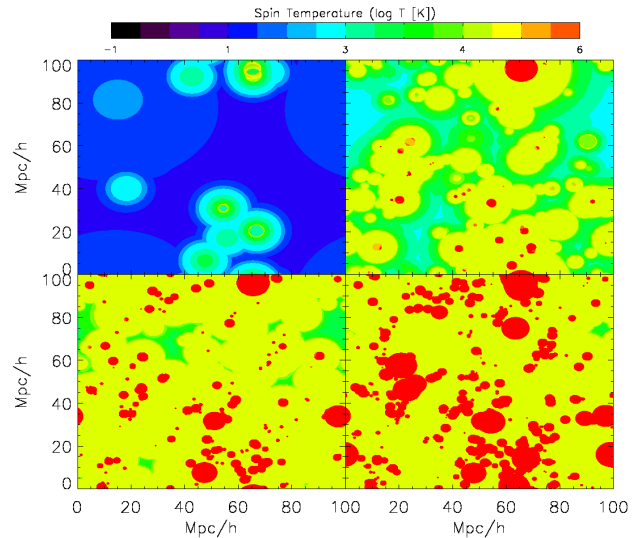
For this hybrid model the number of UV photons was not high enough to ionize the Universe completely by redshift 6 (the ionized fraction reaches 0.95). Full reionization thus could be achieved either by increasing the mass of the black hole and/or by changing the ratio between the black hole and stellar masses.

The hybrid model considered here yielded T_k, T_s and δT_b as in Figs. 8, Fig. 9 and Fig. 10, repectively.

The hybrid model produces heating patterns that interpolates

between the results for the previous two cases and thus is qualitatively different (Fig. 8). The power-law components take over the role of heating an extended region and the stellar component maintains a very high temperature in the central parts.

The spin temperature (Fig. 9) again shows the characteristic ring-like structure around the source. The amount of secondary Lyα radiation produced due to the miniqsos results in an efficient coupling of the spin temperature and the kinetic temperature.

The brightness temperature for the hybrid model is plotted in Fig. 10. The secondary J_o produced due to the power-law component efficiently couples the high ambient T_k of the IGM to T_s
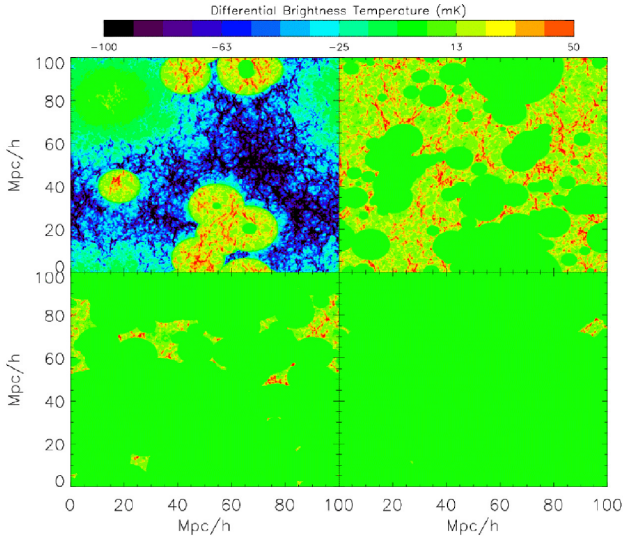
Figure 10. *Differential Brightness temperature for the hybrid model*: Slices correspond to that in Fig. 1. The temperatures (mK) are indicated on a linear scale in the color bar above. The large extent of heating and sufficient J_o ensures that the IGM well beyond the location of the source is rendered visible in 21-cm emission.

and this enables a large fraction of the Universe to be visible in the brightness temperature albeit with a few sources (top-left panel of the figure). The brightness temperature does not go to zero at redshift six because, in the model we have assumed, the Universe is not entirely ionized by then (for recent papers on this issue see Mesinger (2009)).

4.4 Reionization histories: A comparison

In this section we compare the reionization histories for the three scenarios explored above. To create a contigious observational cube or "frequency cube" (right ascension (RA) × declination (DEC) × redshift), we adopt the procedure described in Thomas et al. (2009). The procedure involves the stacking of RA and DEC slices, taken from individual snapshots at different redshifts (or frequency), interpolated smoothly to create a reionization history. This data cube is then convolved with the point spread function of the LOFAR telescope to simulated the mock data cube of the redshifted 21-cm signal as seen by LOFAR. For further details on creating this cube refer to Thomas et al. (2009).

As expected the signatures (both visually and in the r.m.s) of the three scenarios (Fig. 11) are markedly different. In the miniqso-only scenario, reionization proceeds extremely quickly and the Universe is almost completely ($< x_{HII} >= 0.95$) reionized by around redshift 7. The case in which stars are the only source see reionization end at a redshift of 6. Also in this case, compared to the previous one, reionization proceeds in a rather gradual manner. The hybrid model, as explained previously, interpolates between the previous two scenarios.

The δT_b in Fig. 11 is calculated based on the effectivness of J_o, produced by the source, to decouple the CMB temperature (T_{CMB}) from the spin temperature (T_s). This flux, both in spatial extent and amplitude, is obviously much larger in the case of miniqsos compared to that of stars resulting in a markedly higher brightness temperatures in both the miniqso-only and hybrid models when compared to that of the stars. However, we know that stars themselves produce Lyα radiation in their spectrum. Apart

from providing sufficient Lyα flux to their immediate surrounding, this radiation builds up, as the Universe evolves, into a strong background J_o (Ciardi & Madau 2003), potentially filling the Universe with sufficient Lyα photons to couple the spin temperature to the kinetic temperature everywhere. Thus, we plot in Fig. 12 the same set of reionization histories as in Fig. 11 but now assuming that T_s coupled to T_k. Clearly the "cold" regions in the Universe show up as regions with large negative brightness temperature. This assumption though is not strictly applicable towards the beginning of reionization. In §5 we quantify the differences in the brightness temperature evolution when this assumption is made.

It has to be noted that the results we are discussing here are extremely model dependent and any changes to the parametres can influence the results significantly. This on the other is the demonstration of the capability and the need for a "BEARS like" algorithm to span the enormous parametre space of the astrophysical unknowns in reionization studies.

4.5 Looking through LOFAR

To test the feasibiliy of 21-cm telescopes (specifically LOFAR) in distinguishing observational signatures of different sources of reionization, we need to propagate the cosmological 21-cm maps generated in §4.4 using LOFAR's telescope response. The point spread function (PSF) of the LOFAR array was constructed according to the latest configuration of the antenna layouts for the LOFAR-EoR experiment.

The LOFAR telescope will consist of up to 48 stations in The Netherlands [8] of which approximately 22 will be located in the core region (Labropoulos et al. 2009). The core marks an area of 1.7 × 2.3 kilometres and is essentially the most important part of the telescope for an EoR experiment. The core station consists of two sets of antennae, the Low Band (LBA; 30-90 MHz) and the High Band Antenna (HBA; 110-240 MHz). The HBA antennae in the core stations is further split into two "half-stations" of half the collecting area (35-metre diameter), separated by $\approx$ 130 metres. This split further improves the uv-coverage. For details on the antenna layout and the synthesis of the antenna beam pattern refer to upcoming paper by Labropoulos et al. (2009).

In its current configuration, the resolution of the LOFAR-core is expected to be around 3 arcmins. Thus, as an example at redshift 10, all scales below $\approx$ 800 kpc will be filtered out. Fig. 13 shows this effect for the reionization histories corresponding to Fig. 11. The corresponding changes in the r.m.s of the brightness temperature is also plotted. We see that, although smoothed to a large extent, there still exists qualitative differences between the different scenarios. This of course is a reflection of the vastly contrasting models of reionization compared in this paper and difference will disappear if the models investigated are more similar to each another.

5 STATISTICAL ANALYSIS OF THE SIMULATIONS

The previous section provided a qualitative description of the differences in the 21-cm δT_b fluctuations for two cases i.e., with and without the assumption that $T_s = T_k$. In this section, a number of statistical tests are performed to quantify these differences. For this

---

[8] This is decision under review and might change subsequently.
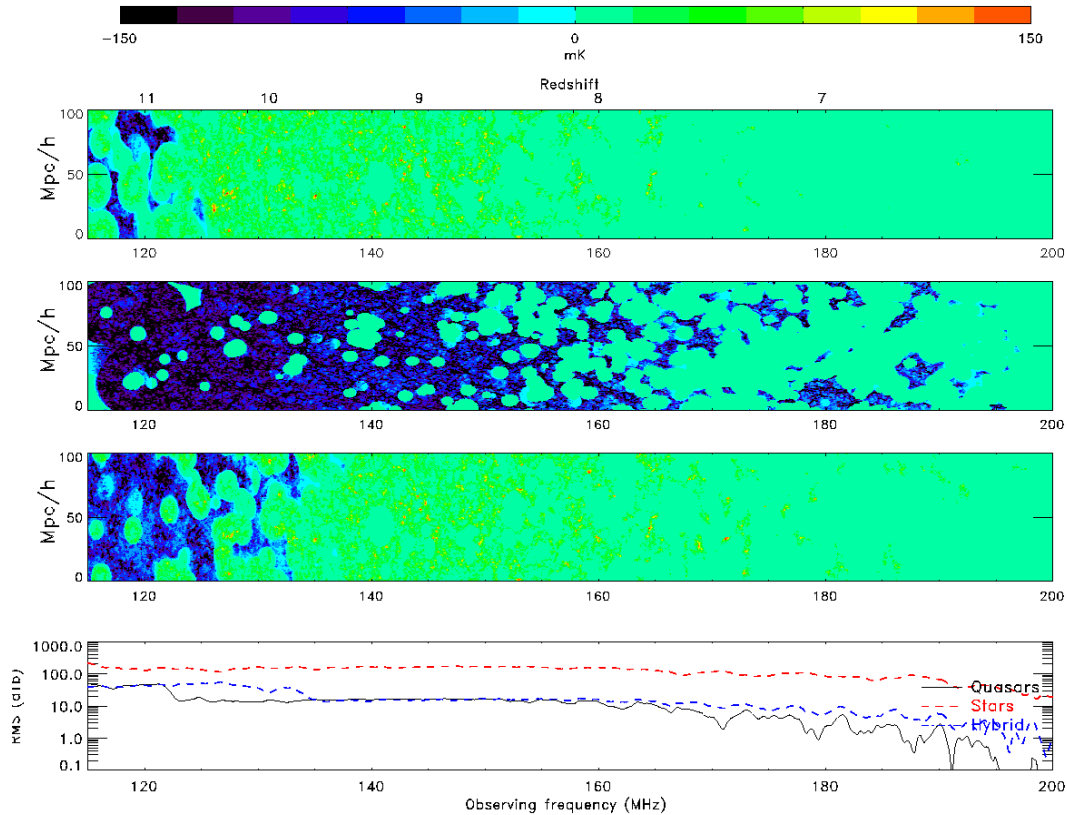
Figure 11. *Contrasting reionization histories*: From the top, reionization histories (δT_b in mK as a function of frequency or redshift) are plotted for miniqso, stellar and hybrid sources, respectively. The bottom panel plots the r.m.s of δT_b as a function of redshift/frequency for all the three cases.

purpose we focus on the scenario with the miniqsos. This exercise can be repeated for the other two scenarios as well.

Firstly, Fig. 14 shows the 3-D power spectra of δT_b at redshift 12, 10, 8 and 6. In our model, reionization begins at around redshift 12.7 and thus z=12 can be considered the onset of reionization. The dashed curve reflects the assumption that $T_s = T_k$ while the solid curve takes into account the evolution of T_s self-consistently. At the initial stages of reionization, only regions at close proximity to the source have been ionized and heated, and the volume filling by "spheres of ionization" has just begun, leaving large portions of the Universe neutral and cooler than the CMB. Here we assume that after the epoch of recombination the Universe cools adiabatically, i.e., $T_k \propto 1/(1+z)^2$ and $T_{CMB} \propto 1/(1+z)$, which results in $T_k \ll T_{CMB}$ at the onset of reionization. Thus, we have a situation in which we have assumed $T_s = T_k$, with $T_k \ll T_{CMB}$, resulting in an *artificial* decoupling of T_s and T_{CMB}, and is manifested as increased 21-cm power. The discrepancy quickly (by $z = 10$) disappears as the "spheres of Lyα" overlap to volume-fill the simulation box and hence increase the T_s — T_k coupling efficiency. Therefore, in our model, it is safe to make the assumption that T_s follows T_k after about $z = 10$.

From Eq. 6 it follows that δT_b attains large negative values when two conditions are satisfied, $T_s \ll T_{CMB}$ and a high neutral hydrogen overdensity. We therefore plot the mean, minimum and maximum values of δT_b as a function of redshift in Fig. 15. As expected the mean and minimum values of δT_b are much lower for the case in which the spin temperature has been set to the kinetic temperature, because the Universe has cooled substantially

below the CMB and coupling T_k everywhere in the Universe to T_s enforces the conditions required for large negative δT_b as stated above. The maximum positive values though do not differ because a positive δT_b indicates that $T_s > T_{CMB}$ and hence has to be heated by the radiating source. And in regions where the source has heated the IGM, the presence of Lyα flux and colliosional coupling almost always guarantees the coupling of T_s to T_k anyway.

As another simple diagnostic of the efficiency of T_s — T_k coupling we plot, (i) the differential temperature, i.e., $1 - T_{CMB}/T_s$, (ii) their ratio, T_k/T_s, as a function of redshift (Fig. 16). Note here that if the spin temperature was artificially set to the kinetic temperature, the differential temperature would be saturated at unity. But the coupling ensures that the spin temperature remains below that of the CMB till about a redshift of 10. Although significantly different at the early phases of reionization, in the model we have assumed, T_s catches up with T_k at a redshift of about eight, when the coupling due to Lyα and collisions become significant enough to tie T_s to the local T_k.

As an alternative probe to investigate the influence of Lyα-coupling coupling, in Fig.17 we plot the power spectra, now of the kinetic (solid line) and the spin (dashed line) temperatures at four different redshifts. There are a few interesting attributes to this figure. Firstly we see that at all scales T_s is considerably lower than T_k at the onset of reionization ($z \approx 12$). This scenario changes rapidly as T_s approaches T_k. Note that it is only towards the end of reionization (z=6) that T_s is identical to T_k at all scales. The pecularity observed is that all scales in T_s do not approach T_k simultaneously. As seen from the top two panels of the figure at
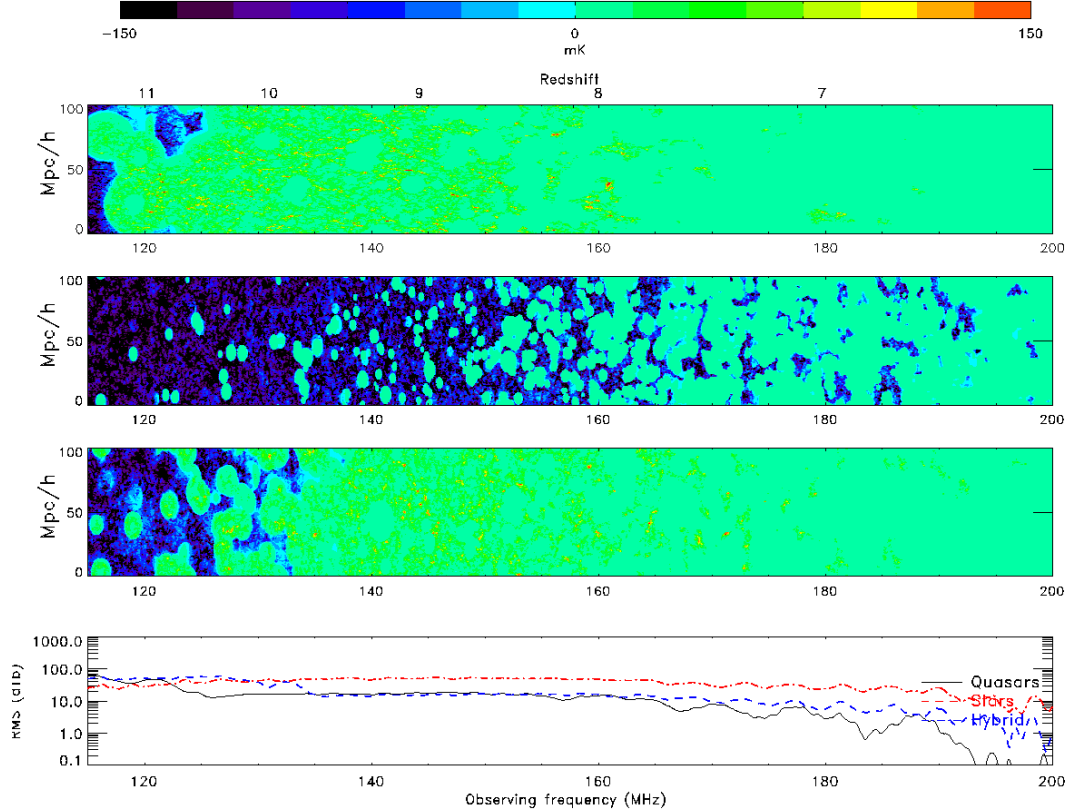
Figure 12. *Reionization histories assuming* $T_s = T_k$: Reionization histories (δT_b), same as in Fig. 11 are plotted, now with the assumption that the T_s has been completely decoupled from T_{CMB}.

$z = 10$ and $z = 8$, T_s approaches T_k at large scales (small k values). And then subsequently at small scales towards the end of reionization. This is because the central parts of the ionized bubble around the source was highly ionized and because $J_o \propto x_{HI}$, the spin temperature obtains extremely low values. Now, as you go further away from the source, the IGM is becomes neutral, but J_o from the source and the secondary Lyα photons is high enough to couple the spin temperature to the kinetic temperature. Thus, the large scales (large volumes outside the ionized bubble) get "matched" first followed by the small scales, when the IGM is hot and collisions become important.

5.1 Comparison to similar work

Here we briefly compare the output of our simulation with that of Santos et al. (2008), wherein a semi-analytical scheme is developed to look at ionization and heating during the epoch of reionization. Fig.18 shows the comparison between our simulations which has now been performed for the case of a power-law source starting at 100eV to facilitate a balanced comparison with the 100eV case of Santos et al. (2008). Plotted in this figure are the average gas temperature (solid line and crosses) and volume filling factor of X-ray radiation (dashed line and filled hexagons). The lines correspond to our simulation and points to Santos et al. (2008). Their case with the normalization factor $f_x = 10$, [9] and photon energies of 100.0

[9] Santos et al. (2008) normalized their spectrum assuming a total integrated power density to be $3.4 \times 10^{40} f_x$ ergs/s/Mpc^3.

eV shows similar trends. Because we start reionization a bit later ($z = 12$) the temperature is a bit lower initially. Their model is qualitatively different because the X-ray emissivity is tied to their star-formation rate. Otherwise, the manner in which heating is implemented to similar to the one described in our case albeit without terms involving compton heating/cooling. These effects though are important towards the central regions of the source (Thomas & Zaroubi 2008).

6 CONCLUSIONS & OUTLOOK

The focus of this paper was three-fold. 1) to introduce an extension to BEARS in order to incorporate heating (including X-ray heating) and discuss its application to two cases of reionization and heating, i.e., for blackbody (stellar) and power-law (miniqso) type sources, 2) to monitor the evolution of spin temperature (T_s) self-consistently and contrast its influence against the usual assumption made in most reionization simulation that $T_s \gg T_{CMB}$, and 3) use the extended BEARS code to study reionization due to a hybrid population of stars and miniqsos as reionizing sources.

To incorporate heating into BEARS, we embedded spheres of "kinetic temperature" around the sources of radiation, much like in the algorithm used to obtain the ionized fraction (Thomas et al. 2009). The BEARS algorithm implemented is extremely fast, in that it takes $\sim$ 5 hours (2GHz, 16-core, 32GB shared RAM) to perform the radiative transfer (including heating) on about 35 different boxes (512^3 and 100 h^{-1} comoving Mpc) between redshifts 12 and 6. These snapshots are interpolated between redshifts to pro-
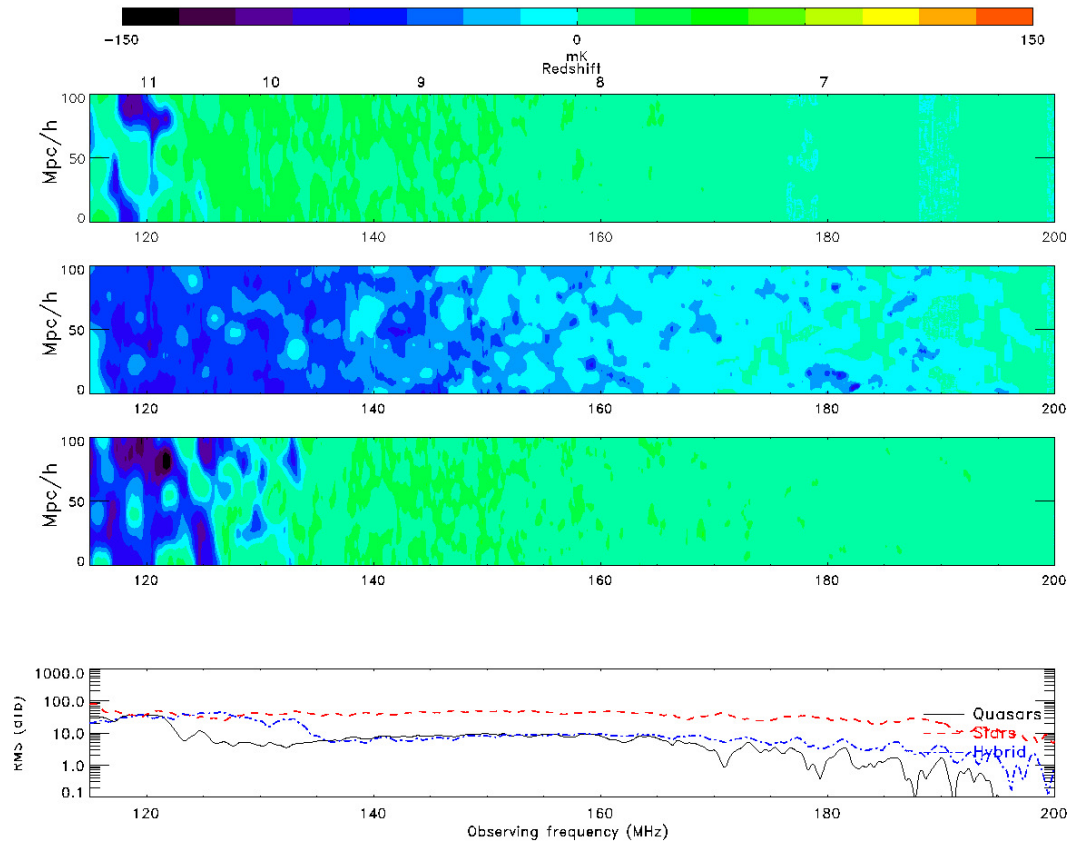
Figure 13. *Convolution with LOFAR - PSF*: Differential brightness temperatures after convolution with a point spread function corresponding to LOFAR is plotted for the same case as in Fig. 11, with the temperatures plotted in mK.

duce a contiguous data cube spanning redshifts $z \approx 6 - 12$, i.e., the observational range of the LOFAR-EoR experiment. The efficiency of the code facilitates the simulation of many different scenarios of reionization and test their observational signatures. Apart from predicting the nature of the underlying cosmological signal, these simulations can be used in conjunction with others probes of reionization to enhance the detectability and/or constrain parameters concerning reionization. In Jelic et al. (2009) these simulations were cross-correlated with the simulations of the CMB anisotropy (mainly the kinetic and thermal SZ-effect) to probe reionization. In the same paper Jelic et al., repeated the same exercise by using reionization simulations from Mellema et al. (2006) and found similar results, further emphasizing the validity of the approximate manner in which we solve the evolution of the kinetic temperature in our simulations.

The improved BEARS code was used to simulate three distinct reionization scenarios, i.e., miniqsos, stellar and a mixture of both. These simulations further emphasized that miniqsos were not only very efficient in increasing T_k of the IGM but the secondary Lyα flux produced by these sources was enough to drive T_s away from T_{CMB} in an extended region around the source thereby rendering the IGM around the source "bright" in δT_b. This implies, if a miniqso hosting a black hole in the mass range $> 10^7 \ M_\odot$ is within the observing window of LOFAR, the value of δT_b and its spatial extent would be conducive to a possible detection. The code was also applied to simulate reionization with a hybrid population of stars and miniqsos. Every dark matter halo was embedded with both a quasar and a stellar component. The relation between the two

was set according to the "Magorrian relation" we observe today. The total mass in quasars were constrained following black hole mass density estimates by Volonteri, Lodato, & Natarajan (2008). The effect of the hybrid population on the IGM was an interpolation between the scenarios of stars and miniqsos i.e., although the heating (and ionization) was not as extended as in the case of miniqsos, it was definitely larger than that for stars.

Our ultimate goal is to simulate mock data sets for the LOFAR-EoR experiment. Towards this end, reionization simulations performed on 35 different snapshots between redshifts 6 and 12 were combined to form "frequency cubes" (reionization histories, Thomas et al. (2009)) for all three scenarios i.e., stars, miniqsos and the hybrid case. To fold-in the effect of the instrument we smoothed these frequency cubes according to the LOFAR beamscale. Notwithstanding the convolution by the LOFAR beam, stark differences between the scenarios clearly persists. The r.m.s δT_b cleary shows this difference between scenarios.

All three scenarios of reionization discussed above was performed for two different cases, i) assuming that T_s is always coupled to T_k and ii) following the evolution of T_s self-consistently in the simulation. Figures 11 and 12 reflect the differences between the two cases. To further quantify the influence of the self-consistent evolution of T_s, especially at the beginning of reionization, a suite of statistical analyses was performed [10]. Firstly, the 3-D power spectra of δT_b (Fig. 14) for the two cases was calcu-

---

[10] Although these tests are specific to the scenario with miniqsos, it can be repeated for the case of stars and the hybrid. Miniqsos were chosen since in
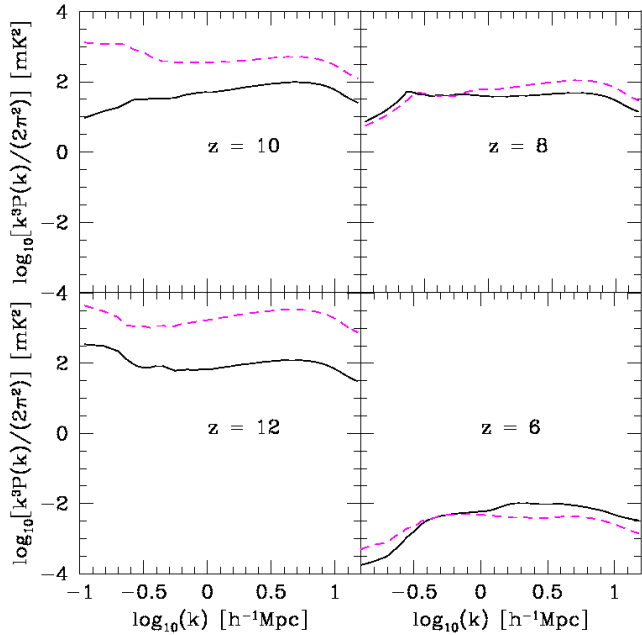
Figure 14. The 3-D power spectra of δT_b at four different redshifts (as indicated on the panels) are plotted. The solid curves indicate the power spectra resulting from the self-consistent inclusion of T_s and the dashed curve, under the assumption $T_s = T_k$. At the onset of reionization, $z \approx 12$ in our model, δT_b is larger at all scales under this assumption because we have enforced, in effect, an *artificial* decoupling of T_s from T_{CMB} in regions of the simulated Universe where $T_k \ll T_{CMB}$. But by redshift 10 the power spectra match exactly as the Lyα becomes efficient everywhere in the box to couple T_s to T_k. Notice that the power keeps dropping as $x_{HI} \to 0$ and Universe gets reionized at lower redshifts.

lated at four redshifts (12, 10, 8 and 6). We see that although there is a considerable difference at the onset (z=12) of reionization the power spectra of the brightness temperature match-up by a redshift of 8. This is attributed to the volume filling nature of the spin temperature coupling induced by miniqsos. The minimum, maximum and mean value of δT_b as a function of redshift reveal similar differences between the two cases. The maximum value of δT_b is the same in both cases because regions where the IGM is considerably heated also corresponds to regions with a large supply of Lyα photons and they are also regions where colliosional coupling is effective. The minimum and average values reveal a difference since under the assumption that $T_s = T_k$, regions much below T_{CMB} are artificially coupled to T_s. As a final statistic we compute the 3-D power spectra of T_k and T_s and compare them (Fig. 17. Vast differences do exist between the two almost till the end of reionization, when they become identical. An interesting result of this comparison is that the large scales of the two spectra get matched before the small scales in the box. The interpretation of this behaviour is given in section 5. We also compared our results to that of Santos et al. (2008) and found good match for the evolution of gas temperature and the volume filling factor of X-ray radiation.

In the near future calibration errors expected from a LOFAR-EoR observational run will be added to these simulations along with the effects of the ionosphere and expected radio frequency

this case we observe the largest difference due to of the copous amounts of secondary Lyα flux and heating induced by miniqsos.
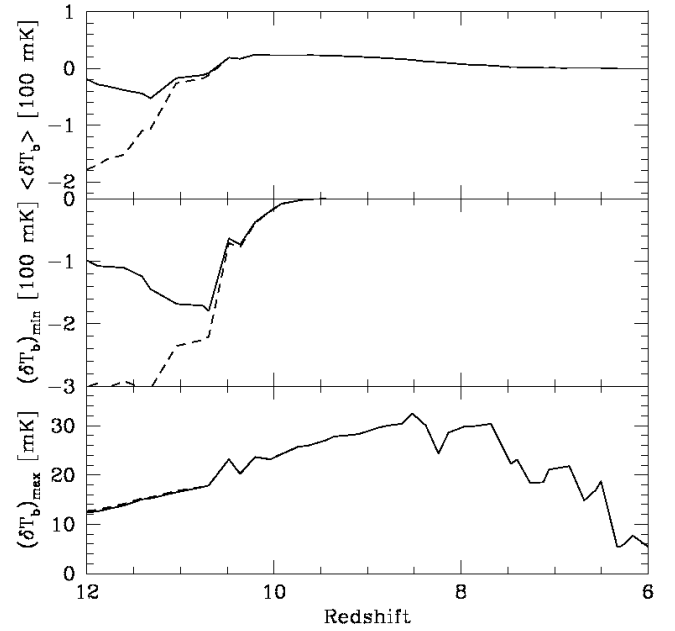
Figure 15. Plotted above are the mean (top), minimum (middle) and maximum (bottom) values of δT_b as a function of redshift. Line styles correspond to Fig.14. Because at earlier redshifts (around 12) $T_k \ll T_{CMB}$ within a large fraction in the simulation box, the minimum value attained by assuming $T_s = T_k$ is much lower than when only regions with Lyα excitation (which is typically near the source) is allowed to couple T_s with T_k. And for the same reason the maximum value in both cases are similar because the assumption holds close to the sources as the presence of Lyα flux ensures efficient coupling. As a result the global average δT_b is also lower for the approximated model at the onset of reionization and catches up quickly to the "proper" model as the Universe fills up with sufficient Lyα flux.

interference (RFI). Subsequently, Galactic and extra-galactic foregrounds modeled as in Jelić et al. (2008) will be merged with these simulations to create the final "realistic" data cube. These data cubes will be processed using the LOFAR signal extraction and calibration schemes being developed to retrieve the underlying cosmological signal in preparation for the actual LOFAR-EoR experiment which has already begun.

7 ACKNOWLEDGMENT

REFERENCES

Abel T., Bryan G. L., Norman M. L., 2002, Science, 295, 93
Abel T., Bryan G. L., Norman M. L., 2000, ApJ, 540, 39
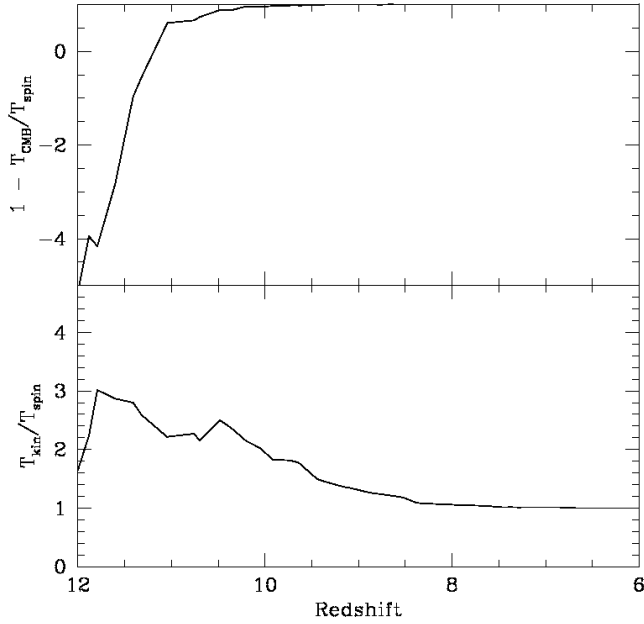
Figure 16. The differential temperature $(T_{spin} - T_{CMB})/T_{spin}$ (top) and the ratio, T_{kin}/T_{spin} (bottom), are plotted as a function of redshift. If T_{spin} was assumed to track T_{kin}, then the top panel would always be saturated at unity. The kinetic temperature likewise merge with the spin temperature only by a redshift of $z = 8$, as seen in the bottom panel.
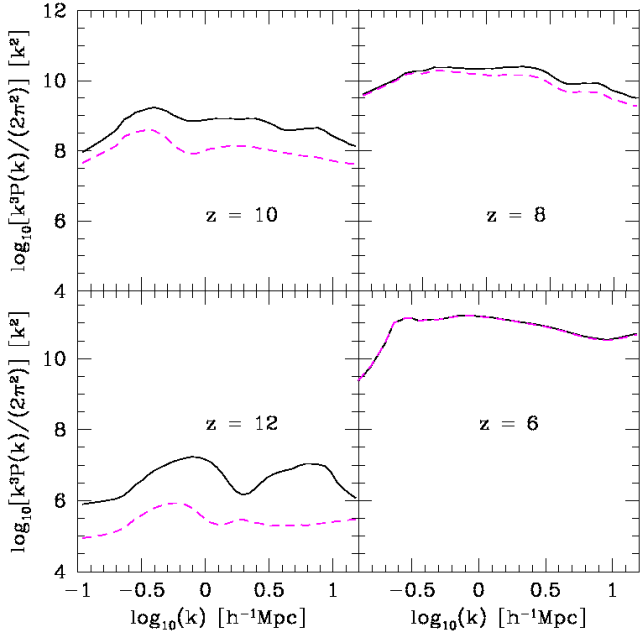
Figure 17. At four different redshifts are plotted the power spectra of the kinetic temperature (solid) and the spin temperature (dashed) within the simulation box. Note how the T_s is considerably lower than the T_k initially and then merges with T_k as reionization proceeds. Refer text for more details.
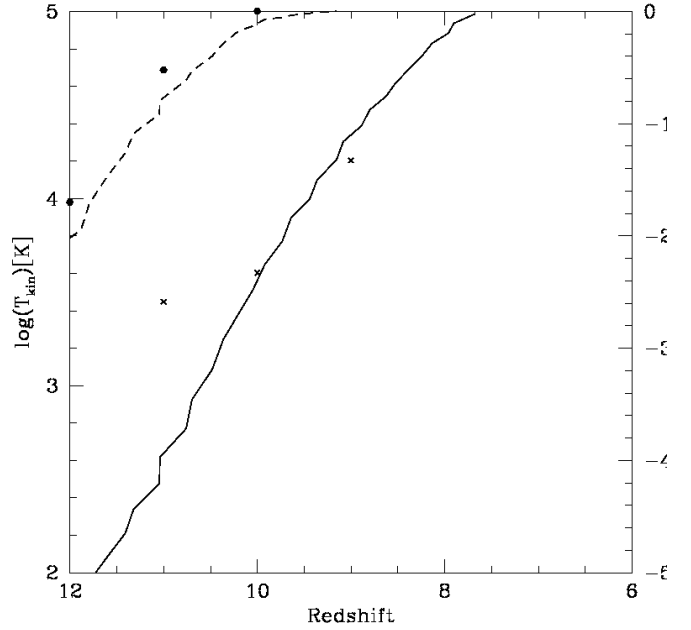
Figure 18. Plotted here are the evolution of the gas temperature T_k (solid line) and the volume filling factor (dashed line) of the X-ray radiation as a function of redshift for the case of the miniqsos. For comparison, points from Santos et al. (2008) are shown for T_k (crosses) and filling factor (filled hexagons) with their case of $f_x = 10$ and photon energies 100.0 eV.

Baek S., Di Matteo P., Semelin B., Combes F., Revaz Y., 2009, A&A, 495, 389

Bromm, V., Coppi, P.S., Larson, R.B., 2002, ApJ, 564, 23

Chuzhoy L., Alvarez M. A., Shapiro P. R., 2006, ApJ, 648, L1

Ciardi B., Madau P., 2003, ApJ, 596, 1

Ciardi B., Ferrara A., Marri S., Raimondo G., 2001, MNRAS, 324, 381

Davis M., Efstathiou G., Frenk C. S., White S. D. M., 1985, ApJ, 292, 371

Dijkstra M., Haiman Z., Loeb A., 2004, ApJ, 613, 646

Elvis M., et al., 1994, ApJS, 95, 1

Gnedin N. Y., Abel T., 2001, NewA, 6, 437

Furlanetto S. R., Zaldarriaga M., Hernquist L., 2004, ApJ, 613, 1

Fan X., et al., 2006, AJ, 131, 1203

Ferrarese L., 2002, ApJ, 578, 90

Field G. B., 1958, Proc I.R.E., 46, 240

Fukugita M., Kawasaki M., 1994, MNRAS, 269, 563

Furlanetto S. R., Loeb A., 2002, ApJ, 579, 1

Jelić V., et al., 2009, arXiv, arXiv:0907.5179

Jelić V., et al., 2008, MNRAS, 891

Kuhlen M., Madau P., 2005, MNRAS, 363, 1069

Laor A., Fiore F., Elvis M., Wilkes B. J., McDowell J. C., 1997, ApJ, 477, 93

Labropoulos P., et al., 2009, arXiv, arXiv:0901.3359

Laursen P., Razoumov A. O., Sommer-Larsen J., 2009, ApJ, 696, 853

Madau P., Meiksin A., Rees M. J., 1997, ApJ, 475, 429

Magorrian J., et al., 1998, AJ, 115, 2285

Mellema G., Iliev I. T., Alvarez M. A., Shapiro P. R., 2006, NewA, 11, 374

Mesinger A., 2009, arXiv, arXiv:0910.4161

Mesinger A., Furlanetto S., 2007, ApJ, 669, 663

Nakamoto T., Umemura M., Susa H., 2001, MNRAS, 321, 593

Nusser A., 2005, MNRAS, 359, 183

Nusser A., Silk J., 1993, ApJ, 411, L1

Page L., et al., 2007, ApJS, 170, 335

Pawlik A. H., Schaye J., 2008, arXiv, 802, arXiv:0802.1715

Pierleoni M., Maselli A., Ciardi B., 2009, MNRAS, 393, 872

Razoumov A. O., Cardall C. Y., 2005, MNRAS, 362, 1413

Ricotti M., Ostriker J. P., 2004, MNRAS, 352, 547

Rijkhorst E.-J., Plewa T., Dubey A., Mellema G., 2006, A&A, 452, 907

Ritzerveld J., Icke V., Rijkhorst E.-J., 2003, astro, arXiv:astro-ph/0312301

Santos M. G., Amblard A., Pritchard J., Trac H., Cen R., Cooray A., 2008, ApJ, 689, 1

Sazonov S. Y., Ostriker J. P., Sunyaev R. A., 2004, MNRAS, 347, 144

Schaerer D., 2002, A&A, 382, 28

Seljak U., Zaldarriaga M., 1996, ApJ, 469, 437

Shull J. M., van Steenberg M. E., 1985, ApJ, 298, 268

Spergel D. N., et al., 2007, ApJS, 170, 377

Springel V., 2005, MNRAS, 364, 1105

Springel V., Hernquist L., 2003, MNRAS, 339, 312

Susa H., 2006, PASJ, 58, 445

Thomas R. M., et al., 2009, MNRAS, 393, 32

Thomas R. M., Zaroubi S., 2008, MNRAS, 384, 1080

Tasitsiomi A., 2006, ApJ, 645, 792

Vanden Berk D. E., et al., 2001, AJ, 122, 549

Vignali C., Brandt W. N., Schneider D. P., 2003, AJ, 125, 433

Volonteri M., Lodato G., Natarajan P., 2008, MNRAS, 383, 1079

Valdés M., Ferrara A., 2008, MNRAS, 387, L8

Whalen D., Norman M. L., 2006, ApJS, 162, 281

Wouthuysen S. A., 1952, AJ, 57, 31

Wyithe J. S. B., Loeb A., 2004, ApJ, 610, 117

Yoshida N., Sokasian A., Hernquist L., Springel V., 2003, ApJ, 598, 73

Zahn O., Lidz A., McQuinn M., Dutta S., Hernquist L., Zaldarriaga M., Furlanetto S. R., 2007, ApJ, 654, 12

Zaroubi S., Thomas R. M., Sugiyama N., Silk J., 2007, MNRAS, 375, 1269

Zaroubi S., Silk J., 2005, MNRAS, 360, L64